Research Article | Vol. 32, No. 7 / 25 Mar 2024 / Optics Express 10862
Optics EXPRESS

Characterization of ultrashort vector pulses from a single amplitude swing measurement

CRISTIAN BARBERO,[1,*] BENJAMÍN ALONSO,[1,2] AND ÍÑIGO J. SOLA[1,2]

[1] Grupo de Investigación en Aplicaciones del Láser y Fotónica (ALF), Universidad de Salamanca, 37008 Salamanca, Spain
[2] Unidad de Excelencia en Luz y Materia Estructuradas (LUMES), Universidad de Salamanca, Spain
[*] cristianbp@usal.es

Abstract: Ultrashort vector pulses exhibit time- and frequency-dependent polarization, sparking significant interest across various fields. Simple, robust, and versatile characterization techniques are crucial to meet this rising demand. Our study showcases how complete polarization dynamics are encoded within a single amplitude swing trace, demonstrated both theoretically and experimentally. We have developed a reconstruction strategy to effectively extract all this information. The amplitude swing technique's sensitivity to vector pulses offers a robust, compact in-line setup adaptable across diverse pulse bandwidths, durations, and spectral ranges. This self-referenced method offers effective measurement of ultrashort vector pulses, addressing the growing interest in these complex pulses.

1. Introduction

Laser pulses with time-varying polarization, i.e., vector pulses, are becoming more and more essential in applications due to allowing an enhanced understanding and control of diverse physics phenomena, including coherent control of certain light-matter interactions [1,2], post-compression of pulses [3,4], polarization dynamics of dissipative solitons in fiber lasers [5,6], ultrafast structured light [7,8], or high-order harmonic generation [9]. In these applications, the characterization of those complex pulses is fundamental for their optimization.

Several techniques have been developed for measuring constant linearly polarized pulses, such as FROG [10], SPIDER [11], d-scan [12], or, more recently, amplitude swing (a-swing) [13] and frequency-resolved optical switching (FROSt) [14]. In a more general case, the polarization state of a vector pulse depends on the relative amplitude and phase between their two pulse projections. In general, these techniques are not sensitive to the zero- and first-order terms of the spectral phase (related to the carrier-envelope phase and the arrival time of the pulse), so it is not enough to independently measure two orthogonal polarization projections to characterize a vector pulse, since the relative phase among the two polarization components is missed.

Consequently, other strategies have emerged. POLLIWOG [15] is based on dual-channel spectral interferometry (SI). Both polarization projections are split and interfere with the corresponding projections of the same reference pulse, thus obtaining their relative phase [16]. Measuring the reference pulse with any scalar technique, the vector pulse is fully reconstructed. In Ref. [17], SI is also used, with an in-line single-channel implementation through a bulk interferometer that overcomes the stability requirement. In this case, the relative phase is obtained from the interference between two common projections of the pulse (eliminating the need of an additional reference pulse), while one of the components is measured with any scalar technique. TURTLE [18] proposes another approach, based on measuring three polarization projections (with any scalar method). Two orthogonal pulse components are characterized by two of those measurements, and the third one provides the relative phase between them. Recently, a similar approach has been presented for d-scan, using a third fundamental spectrum projection to

#515198 https://doi.org/10.1364/OE.515198
Journal © 2024 Received 11 Dec 2023; revised 21 Feb 2024; accepted 25 Feb 2024; published 11 Mar 2024

Optics EXPRESS

obtain the relative linear phase [19]. DFG-XTURTLE [20] combines TURTLE and XFROG [21] to characterize vector pulses in the ultraviolet range. Time-resolved ellipsometry [22], chip-integrated plasmonic [23], and nanointerferometric [24] measurements also characterize vector pulses but are less utilized than the previous techniques due to their greater complexity.

Those spectral interferometric methods require a known scalar reference pulse, i.e., they need two (or more) measurements to reconstruct a vector pulse: one to characterize the reference scalar pulse, and other to obtain the relative phase between the two polarization components. We show here that a-swing encodes all the information required to fully characterize a vector pulse in a single trace, thus serving as a self-referenced method. This technique presents a simple in-line configuration, with common optical elements, and easily adaptable for a broad range of pulse durations and bandwidths [13,25]. These characteristics confer robustness, simplicity, and versatility to the system. Recently, it has been shown that a-swing can characterize pulses in different spectral bands over more than an octave with the same setup [26], and employing diverse modulating functions [27].

In this work, we firstly investigate analytically the a-swing trace expression for a vector input pulse and perform simulations to show that this trace encodes the spectral phases of both components, including their relative phase. To extract this information from the trace, we developed a new reconstruction strategy based on a nonlinear optimization algorithm, detailed in Section 3. Next, we present experimental measurements and their corresponding reconstructions, validated with simulations. Lastly, we discuss the conclusions.

2. Vector pulse measurement: amplitude swing

2.1. Amplitude swing for scalar pulses

For our purpose of measuring vector pulses from a single measurement, we will be based on the a-swing technique. A-swing consists in generating two replicas of the unknown scalar pulse with a fixed time delay between them, while varying their relative amplitude. For each relative amplitude, the spectrum of the signal of a nonlinear interaction with matter (e.g., second harmonic generation, SHG) of the interference pulse is recorded, thus obtaining a two-dimensional trace [Eq. (1)]. This trace encodes the input pulse spectral phase, from which the pulse can be retrieved [13,25]. This can be achieved by using the experimental setup presented in Fig. 1. The input pulse (horizontal linear polarization in this example) passes through a rotating multiple-order waveplate (MWP), generating the two delayed replicas, whose relative amplitude depends on the MWP axes orientation, θ (angle between MWP fast axis and horizontal axis). A linear polarizer (LP) selects one polarization projection of the MWP pulse, which then generates a nonlinear signal, recorded by a spectrometer for each angle θ, obtaining a trace given by:

$$S^{SHG}(\omega,\,\theta) = \left| \int \left(\int E(\omega')[\cos^2\theta\, e^{i\rho_f(\omega')} + \sin^2\theta\, e^{i\rho_s(\omega')}]\, e^{i\omega' t}\, d\omega' \right)^2 e^{-i\omega t}\, dt \right|^2 \qquad (1)$$

where $E(\omega)$ represents the input pulse, and $\rho_f(\omega)$ and $\rho_s(\omega)$ are the spectral phases acquired by the fast and slow pulse replicas after propagating through the MWP.

2.2. Amplitude swing applied to vector pulses

To measure vector pulses, we have chosen the original implementation of a-swing (Fig. 1) because of its simplicity and versatility described before, and since it intrinsically deals with vector pulses, manipulating the pulse polarization in the rotating MWP. Notice that this is not a sufficient condition, as other techniques can manage polarization without measuring vector pulses (e.g., compact FROG [28] and SPIDER [29] versions, or self-referenced SI [30]).

Optics EXPRESS

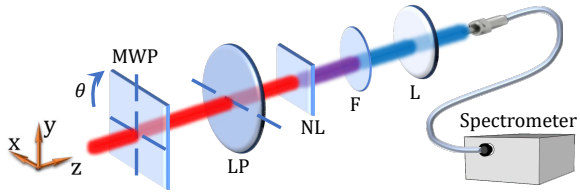

Fig. 1. A-swing experimental setup scheme: multiple-order waveplate (MWP), whose fast axis is rotated at an angle θ with respect to the x-axis; linear polarizer (LP), with the transmission axis horizontal; nonlinear crystal (NL); fundamental signal filter (F); and convergent lens (L). A fiber-coupled spectrometer collects the nonlinear signal.

The input pulse to be measured is a vector pulse with horizontal —$E_{\mathrm{x}}(\omega)$— and vertical —$E_{\mathrm{y}}(\omega)$— polarization components described as:

$$\begin{pmatrix} E_x(\omega) \\ E_y(\omega) \end{pmatrix} = \begin{pmatrix} A_x(\omega)\, e^{i\,\varphi_x(\omega)} \\ A_y(\omega)\, e^{i\,\varphi_y(\omega)} \end{pmatrix} \tag{2}$$

where $A_{\mathrm{x,y}}(\omega)$ and $\varphi_{\mathrm{x,y}}(\omega)$ are their spectral amplitudes and phases, respectively. The MWP introduces the phases $\rho_{\mathrm{f}}(\omega)$ and $\rho_{\mathrm{s}}(\omega)$ to the fast and slow replicas, respectively, so the pulse in the MWP axes coordinates is:

$$\begin{pmatrix} E_f^{MWP}(\omega,\,\theta) \\ E_s^{MWP}(\omega,\,\theta) \end{pmatrix} = \begin{pmatrix} [E_x(\omega)\cos\theta + E_y(\omega)\sin\theta]\, e^{i\,\rho_f(\omega)} \\ [-E_x(\omega)\sin\theta + E_y(\omega)\cos\theta]\, e^{i\,\rho_s(\omega)} \end{pmatrix} \tag{3}$$

and rewritten in the x- and y- axes is:

$$\begin{pmatrix} E_x^{LP}(\omega,\,\theta) \\ E_y^{LP}(\omega,\,\theta) \end{pmatrix} = \begin{pmatrix} E_x(\omega)[\cos^2\theta\; e^{i\,\rho_f(\omega)} + \sin^2\theta e^{i\,\rho_s(\omega)}] \\ +E_y(\omega)\cos\theta\sin\theta[\; e^{i\,\rho_f(\omega)} - \; e^{i\,\rho_s(\omega)}] \\ E_x(\omega)\cos\theta\sin\theta[\; e^{i\,\rho_f(\omega)} - \; e^{i\,\rho_s(\omega)}] \\ +E_y(\omega)[\cos^2\theta\; e^{i\,\rho_s(\omega)} + \sin^2\theta e^{i\,\rho_f(\omega)}] \end{pmatrix} \tag{4}$$

After the MWP, the LP selects one projection of this pulse —in this case the horizontal one, $E_{\mathrm{x}}^{\mathrm{LP}}(\omega,\,\theta)$—, which is the result of the interference of four components, whose amplitudes are modulated by θ: horizontal fast (E_{xf}), vertical fast (E_{yf}), horizontal slow (E_{xs}), and vertical slow (E_{ys}), defined as:

$$\begin{aligned} E_{xf}(\omega,\theta) &= E_x(\omega)\,\cos^2\theta\; e^{i\,\rho_f(\omega)} \\ E_{yf}(\omega,\theta) &= \; E_y(\omega)\;\cos\theta\sin\theta e^{i\,\rho_f(\omega)} \\ E_{xs}(\omega,\theta) &= E_x(\omega)\,\sin^2\theta\; e^{i\,\rho_s(\omega)} \\ E_{ys}(\omega,\theta) &= -\,E_y(\omega)\;\cos\theta\sin\theta e^{i\,\rho_s(\omega)} \end{aligned} \tag{5}$$

The SHG spectrum of this interference pulse for different orientations of the MWP, $S_{\mathrm{x}}^{\mathrm{SHG}}(\omega,\,\theta)$, is the a-swing trace, given by:

$$S_x^{SHG}(\omega,\,\theta) = |E_x^{SHG}(\omega,\,\theta)|^2 = \left| \int \left(\int E_x^{LP}(\omega',\,\theta)\, e^{i\omega' t}\, d\omega' \right)^2 e^{-i\omega t}\, dt \right|^2 \tag{6}$$

Optics EXPRESS

The SHG pulse can be written as:

$$\begin{aligned} E_x^{SHG}(\omega,\,\theta) = & X_{ff}(\omega)\cos^4\theta + [C_{xf,yf}(\omega) + C_{xf,ys}(\omega)]\cos^3\theta\sin\theta \\ & + [Y_{ff}(\omega) + Y_{fs}(\omega) + Y_{ss}(\omega) + X_{fs}(\omega)]\cos^2\theta\sin^2\theta \\ & + [C_{xs,yf}(\omega) + C_{xs,ys}(\omega)]\cos\theta\sin^3\theta + X_{ss}(\omega)\sin^4\theta \end{aligned} \tag{7}$$

where X coefficients are related to the SHG of E_x, Y coefficients to the SHG of E_y, and C

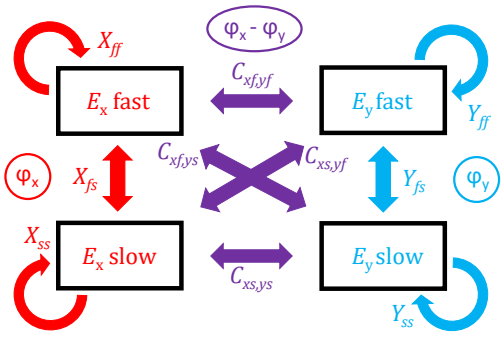

Fig. 2. Terms involved in the SHG signal that constitutes the a-swing trace. The pulse that generates this nonlinear signal has four components (represented inside the rectangles), and each possible combination between them (ten in total, represented by arrows) leads to a term of the SHG pulse [Eq. (7)]. Red (blue) arrows indicate the terms associated with the horizontal (vertical) projection of the vector pulse, which encodes φ_x (φ_y); whereas purple arrows indicate the crossed terms, which encode the relative phase ($\varphi_x - \varphi_y$).

coefficients to the SHG of the crossed terms of E_x and E_y; while the subscripts f and s indicate the fast and slow replicas, respectively. From the point of view of the laboratory reference system, the nonlinear signal presents three terms associated with the horizontal projection, three with the vertical projection, and four crossed terms. On the other hand, from the point of view of the MWP replicas, it presents three terms related to the fast replica, three to the slow replica, and four crossed terms. These interrelationships between the pulse components are illustrated in Fig. 2, from which it is deduced how the trace encodes the individual spectral phases of both components (encoded in the individual interference of X and Y coefficients, respectively), and their relative phase (due to the interferences between E_x and E_y pulses, encoded in C coefficients). We have corroborated this assumption by numerical simulations with different input vector pulses (see Supplement 1, Fig. S1 and S2), also confirming the absence of ambiguities regarding the signs of the phases of the polarization components. This analysis is essential to understand that despite measuring the SHG of a single projection, it encodes the full vector pulse information. In the case of x- (y-) linearly polarized pulses, the components of the SHG pulse are reduced to X_{ff}, X_{fs}, and X_{ss} (Y_{ff}, Y_{fs}, and Y_{ss}), and thus the corresponding SHG spectrum of the a-swing trace presents six terms (all possible combinations of these three SHG pulses, as shown in Ref. [13]). Analogously, the SHG spectrum generated with vector pulses is constituted by 55 terms, resulting from all the combinations with repetition of sets of two elements from the ten SHG pulse components [Eq. (7)], i.e., $\binom{10+2-1}{2} = 55$.

Thus, the polarization state of the vector input pulse is encoded in the a-swing trace. This sensitivity to vector pulses is inherent to the concept of amplitude modulation of the replicas of the pulse components, independent of the particular implementation that we show here using a

Optics EXPRESS

bulk polarization interferometer (MWP and LP). As usual, the information cannot be analytically extracted, so a devoted reconstruction algorithm is needed.

3. Reconstruction algorithm

To characterize the vector pulse, we have implemented a new dedicated strategy —presented in this section— that follows several steps to retrieve the full pulse information. As said before, the input pulse is defined referred to two polarization components, E_x and E_y [Eq. (2)]. Both spectral amplitudes are obtained from the measured spectra, as $A_{x,y}(\omega) = \sqrt{S_{x,y}(\omega)}$. The spectral phases —$\varphi_x(\omega)$ and $\varphi_y(\omega)$— are the unknown functions to be recovered by the retrieval algorithm from the a-swing trace. From each pulse spectral amplitude and phase, we calculate the temporal intensity $I(t)$ and phase $\phi(t)$, showing in the results (Section 4) the intensity and phase in both domains.

For application in the retrieval algorithm, the a-swing trace can be simulated for a given vector pulse, which will be reconstructed afterwards. Since the origin of the time axis can be defined arbitrarily, and a global constant phase does not modify the pulse envelope, we force to zero the phase offset —$\varphi_0 = \varphi(\omega_0)$— and the time for the maximum of the pulse (related to the arrival time or delay τ, i.e., to the spectral phase linear term) of $E_x(\omega)$, thus the zero- and first-order relative phases —$\Delta\varphi_0 = \varphi_{0x} - \varphi_{0y}$ and $\Delta\tau = \tau_x - \tau_y$ (positive $\Delta\tau$ means that the y-component arrives before the x-component)— are codified in $\varphi_y(\omega)$. The spectral phases introduced by the MWP —$\rho_f(\omega)$ and $\rho_s(\omega)$— depend on the ordinary and extraordinary refractive indices, which are known since they can be calculated from their respective Sellmeier equations [31], and the MWP thickness, which is given by the manufacturer or calibrated using in-line SI [17], for instance. Analogously, the dispersion of the other elements of the setup can be considered within the reconstruction algorithm, so that it does not affect to the input pulse retrieval. The SHG field is simulated by squaring the pulse in the temporal domain, assuming a flat spectral response on the nonlinear crystal. The calculated signal is the spectrum of the SHG pulse as a function of the MWP orientation (the simulated a-swing trace).

Different algorithms have been employed in spectral phase retrievals of scalar pulse measurements, such as Nelder-Mead Simplex [12], projections [32], differential evolution [26,33], and neural networks [34,35]. In the literature it is shown that the Levenberg-Marquardt algorithm [36,37] is robust reconstructing scalar pulses from d-scan [38–40] and a-swing [13,25,27] measurements, so we choose this algorithm but any other could be used in principle. It is a well-known nonlinear optimization constrained algorithm to invert multivariable problems, in which the spectral phase is parametrized, and it is iteratively modified while minimizing a merit function, which is the square of the difference between simulated and experimental traces.

The reconstruction strategy runs several consecutive optimization steps (lasting a few minutes in total), whose outputs are used as a seed for the following optimization. In the first step, an initial guess of $\varphi_x(\omega)$ is quickly retrieved using only the angles of the trace $\theta = n\pi/2$ (being n an integer) and their adjacent angles. The reason is that at these MWP angles the SHG signal depends only on $E_x(\omega)$ [see Eq. (4), (5) and (6)] due to the amplitude modulation on θ. Because of the LP orientation (0°), the contribution of $E_x(\omega)$ on the trace is greater than the contribution of $E_y(\omega)$. For other LP orientations, the vector pulse information is also encoded on the trace, but the relative weights of both components change. To do this, we parametrize $\varphi_x(\omega)$ with a Taylor expansion up to order three (i.e., group delay dispersion, GDD, and third-order dispersion, TOD), and we optimize it starting with a random guess phase. In the second stage, in which the same part of the trace is used, the spectral phase $\varphi_x(\omega)$ is upgraded by optimizing the values of its discretized derivative in 32 equally spaced points along the frequency axis, while interpolating in the rest of the frequency interval. In the third and fourth steps, we reconstruct $\varphi_y(\omega)$, including the parameters $\Delta\varphi_0$ and $\Delta\tau$ as mentioned before, using the full trace (the whole MWP scan in θ).

Optics EXPRESS

In the third step it is parametrized by a Taylor expansion (fast optimization), while in the fourth one we optimize its derivative values, reducing the frequency sampling to 30 points.

In the fifth and sixth stages, we refine individually the derivative values of both spectral phases $\varphi_x(\omega)$ and $\varphi_y(\omega)$, respectively. Lastly, in the seventh step, we run a simultaneous optimization of the derivative values of both spectral phases, reducing each component sampling to 16 points (plus $\Delta\varphi_0$ and $\Delta\tau$). The relative amplitude between the x and y fundamental spectra can be experimentally calibrated or optimized in the algorithm if needed.

This reconstruction strategy has been firstly validated with simulated traces (see Supplement 1, Fig. S3), and later applied and validated with experimental traces as shown in the next section.

4. Experimental setup and results

4.1. Vector pulses generation

To apply the proposed vector pulse measurement and reconstruction, we firstly generated the vector pulses to be measured, which could come from any experiment of shaping setup. In our case, we produced them by propagating horizontal linearly polarized laser pulses through a shaping system (independent of the a-swing detection explained in Section 2). It consists of a retarder plate (or two consecutive plates), where we define θ_g as the orientation of its fast axis with respect to the horizontal axis (Fig. 3). The scalar feeding pulses preceding vector shaping —central wavelength at ~800 nm, Fourier-limited pulse duration of ~60 fs (full-width at half maximum, FWHM), 5 kHz repetition rate, and ~0.2 mJ per pulse— are emitted by a Ti:sapphire chirped pulse amplification (CPA) system (Spitfire ACE, Spectra Physics).

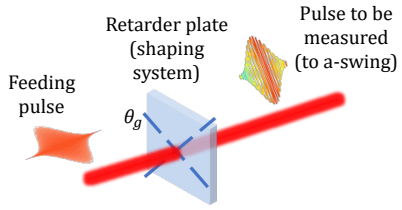

Fig. 3. Experimental generation of the vector pulses to be measured, using a retarder plate (or two consecutive) as shaping system.

Just for validation purposes of the later a-swing reconstructions, we will simulate those vector pulses. To do this, we need to know the feeding pulse and the shaping system. We firstly measured the scalar feeding pulse (Fig. 4) delivered by the laser, using the conventional a-swing [13]. Note that this pulse is not Fourier-limited, but it presents small negative GDD and TOD, being broadened to a duration of 86 fs (FWHM). Then, we simulate its propagation through the retarder plate (using Sellmeier equations and obtaining its thickness through in-line SI experimental calibration [17]) at the corresponding angle θ_g to calculate the vector pulse. The shaping plates were calibrated for the pulse simulation —validation purpose— but note that this is not necessary for the a-swing reconstruction.

In a first experiment, the vector pulses to be measured were generated in the shaping system with a 2-mm quartz retarder plate (delay of 65.6 fs and phase retardation of 0.34π for 800 nm) in different orientations ($\theta_g = 15°, 30°, 45°$). To further test our proposal, we generated in a second experiment a vector pulse using two consecutive retarder plates (5 mm of quartz in total), both oriented at $\theta_g = 45°$, introducing a global 160.9 fs delay and 1.30π phase retardation (for 800 nm). The phase retardations are given subtracting the $2\pi m$ term associated with the order of the plate m, as it can be calculated from the delay and is not relevant to define the effect of the phase in the pulse.

Optics EXPRESS

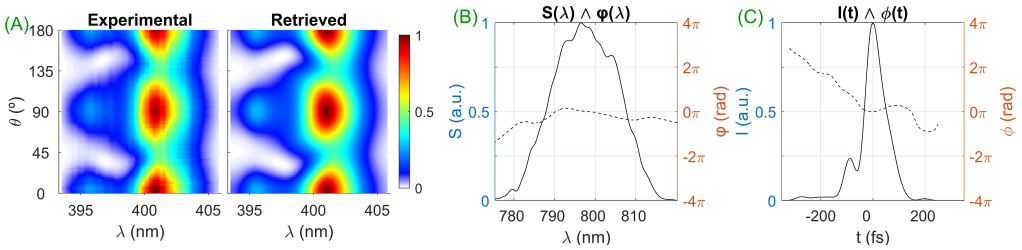

Fig. 4. Measurement of the scalar feeding pulse with a-swing: (A) experimental and retrieved traces; (B) experimental spectrum (solid) and reconstructed spectral phase (dashed); (C) temporal intensity (solid) and phase (dashed) of the retrieved pulse, whose duration (FWHM) is inset.

4.2. *Vector pulses measurement*

The vector pulses generated in that way are afterwards measured with the a-swing detection, shown in Fig. 1. As explained in Section 2, the vector pulses to be measured propagate through a rotating MWP (the rotation angle is scanned in steps of 2°), splitting both polarization projections in fast and slow replicas, whose amplitudes are modulated by θ. The MWP used for the a-swing detection (quartz, 2-mm thickness) introduces a known delay of 65.6 fs between the fast and slow pulses, and a known phase retardation of 0.34π (remember that the $2\pi m$ term is subtracted) for 800 nm (previously calibrated with in-line SI [17]). This delay must be of the order of the Fourier-limited pulse duration with a remarkable tolerance up to three times larger or smaller (notice that this condition does not apply to the actual duration of an eventually chirped pulse), while the phase retardation can be chosen arbitrarily, as discussed in Refs. [13,25]. A LP selects the horizontal projection of the MWP output pulse, which then passes through a type-I BBO nonlinear crystal (20-μm thickness) for the SHG process. The remaining fundamental signal is filtered out with a second LP (F). The SHG radiation, focused with a lens (L) to enhance the signal/noise ratio, is collected by an optical fiber connected to a spectrometer (HR4000, Ocean Optics Inc.), integrating multiple pulses at each MWP angle. The fundamental spectra are recorded with another spectrometer (AvaSpec 2048-USB1, Avantes Inc.). Since the response of the detection system (fiber plus spectrometer) is different for horizontal and vertical axes, the relative amplitude has been set as an unknown in the retrieval algorithm (this response can also be calibrated with a ±45° linearly polarized input pulse). From the a-swing measurement, the studied vector pulses are reconstructed. As said before, these reconstructed vector pulses will be compared with the simulated vector pulses.

For each pulse generated in the first experiment (2-mm quartz retarder plate with different orientations as shaping system, see Section 4.1), we present the experimental and retrieved traces for θ_g values of 15°, 30°, and 45° (the root mean square (rms) errors are 1.83%, 2.10%, and 2.75%, respectively) [Fig. 5(A)], and the comparison between the simulated and retrieved intensity and phase of the vector pulses (both x- and y-component) in the spectral and temporal domains [Fig. 5(B) and 5(C)], as given by Eq. (2) and its inverse Fourier-transform. The spectra in x- and y-axis presents frequencies of null intensity due to the interference between the fast and slow pulses in the retarder plate, so the spectral phase exhibits a π discontinuity (where the phase derivative is infinite). This is more demanding for the retrieval algorithm than a continuous phase. However, when these modulations cause only one frequency of null intensity, as in the 2-mm quartz retarder plate (Fig. 5), it is possible to reproduce these π discontinuities, finding a good agreement between the simulated and retrieved pulses.

In the case of the second experiment (two consecutive retarder plates as shaping), the x- and y-spectra are very modulated (both present three zeros) due to the higher delay, not being possible

Optics EXPRESS

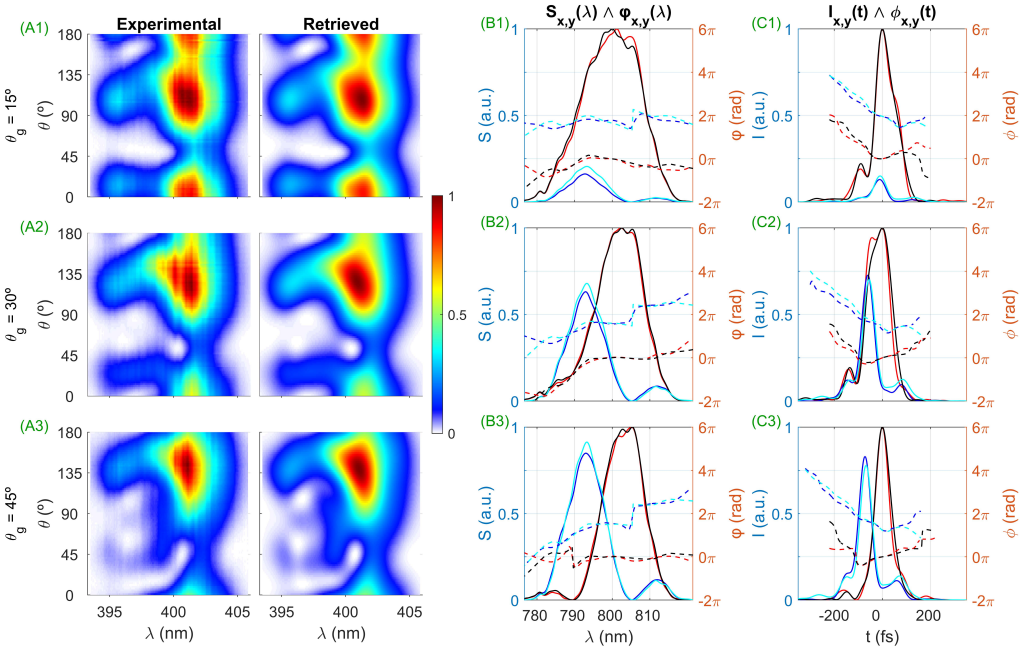

Fig. 5. Experimental a-swing results and comparison with simulations of vector pulses generated by a retarder plate (65.6 fs delay and 0.34π phase retardation) whose axis orientation is 15° (first row), 30° (second row), and 45° (third row): (A) experimental and retrieved traces; (B) experimental and simulated spectra (solid), and reconstructed and simulated spectral phases (dashed); (C) temporal intensities (solid) and phases (dashed) of the retrieved and simulated pulse components. Red: horizontal retrieved; blue: vertical retrieved; black: horizontal simulated; cyan: vertical simulated.

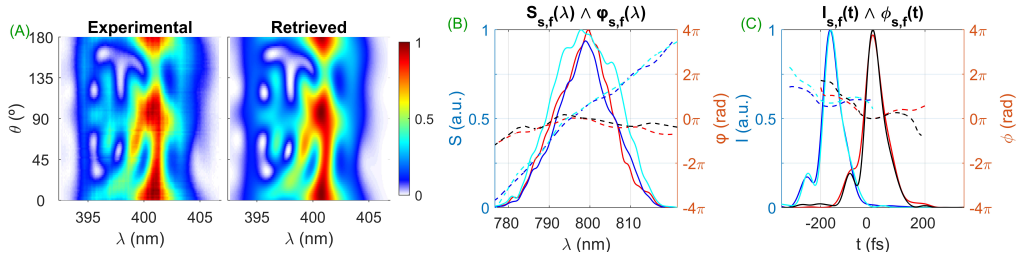

Fig. 6. Experimental a-swing results and comparison with simulations of a vector pulse generated by two consecutive retarder plates (160.9 fs delay and 1.30π phase retardation) whose axis orientation is 45°: (A) experimental and retrieved traces; (B) experimental and simulated spectra (solid), and reconstructed and simulated spectral phases (dashed); (C) temporal intensities (solid) and phases (dashed) of the retrieved and simulated pulse components. Red: -45° (slow) retrieved; blue: 45° (fast) retrieved; black: -45° simulated; cyan: 45° simulated. Simulated spectra of the pulse at 45° and -45° are the same.

Optics EXPRESS

to reconstruct the spectral phase with our current frequency sampling (32 points) in the retrieval algorithm. To overcome this issue, we perform the measurements (Fig. 6) rotating -45° our coordinate system (it coincides with the coordinate axes of the retarder plates, but it is not a requirement). The spectra at -45° (x', slow) and 45° (y', fast) do not present zeros [Fig. 6(B)], enabling to reconstruct the vector pulse using the same retrieval strategy, and with minimum experimental modifications (just rotate the optical elements). Although this issue has been easily overcome here by rotating the coordinate system, it would be interesting in the future to study new retrieval strategies. Even though the x' and y' pulse components hardly overlap in time [Fig. 6(C)], their relative phase is so far encoded in the trace [Fig. 6(A)]. In the same line, numerical simulations (see Supplement 1, Fig. S2, row 3) confirm that the a-swing trace depends on the relative phase even if there is no temporal overlap at all. The agreement between simulated and retrieved pulses is good (the rms error between the traces is 3.41%), evidencing the capability to fully reconstruct vector pulses with a single a-swing trace.

Since the reconstruction provides the full vector pulse information, we have calculated the parameters that characterize the polarization ellipse (variable in time and frequency) for the pulses: the ellipticity ε (defined as the ratio between the minor and major axis, while its sign indicates the helicity, positive for right-handed and negative for left-handed polarization) and the azimuthal angle χ (the orientation of the polarization ellipse: angle between its major axis and the x-axis), showing the results in Fig. 7 and 8. Regarding the polarization state, for $\varepsilon = \pm 1$ it corresponds to circular polarization with said helicity, while $\varepsilon = 0$ identifies linear polarization.

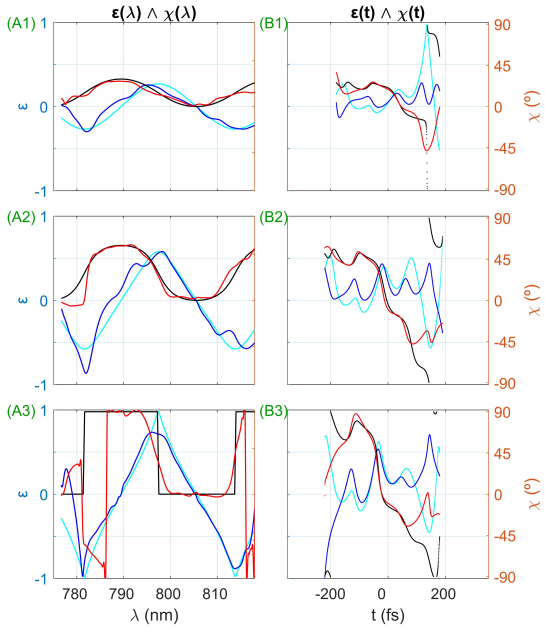

Fig. 7. Polarization ellipticity and azimuth in spectral (A) and time domain (B) of the vector pulses generated with a 2-mm quartz retarder plate (65.6 fs delay), being its axis orientation 15° (first row), 30° (second row) and 45° (third row). Red: retrieved azimuth; blue: retrieved ellipticity; black: simulated azimuth; cyan: simulated ellipticity.

The ellipticity and the azimuth vary periodically along the wavelength axis [Fig. 7(A) and 8(A)]. The relative amplitude between the fast and slow replicas in the retarder plate is $\beta = \tan\theta_g$, which is constant. Thus, for the wavelengths that satisfy $\Delta\varphi(\omega) = \pi m$, the ellipticity is zero and the azimuth is zero (even values of m do not modify the polarization, which corresponds to

Optics EXPRESS

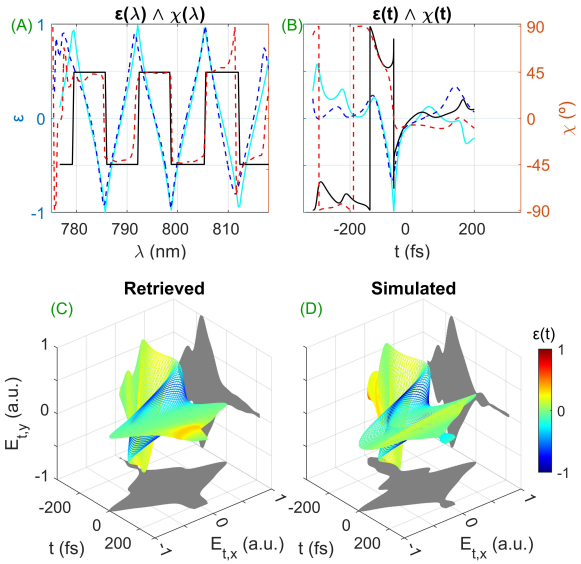

Fig. 8. Polarization ellipticity and azimuth in spectral (A) and time domain (B) of the vector pulse generated with two consecutive retarder plates (160.9 fs delay) oriented at 45°. Red: retrieved azimuth; blue: retrieved ellipticity; black: simulated azimuth; cyan: simulated ellipticity. Retrieved (C) and simulated (D) vector electric field in the temporal domain, with their corresponding projections in gray color. The color scale indicates the ellipticity, being -1 and +1 left- and right-handed circular polarization, respectively, and 0 linear polarization).

$A_y(\omega) = 0$) or maximum ($\chi = 2\theta_g$, odd m values, due to operation as half-wave plate for that wavelength), i.e., the pulse is linearly polarized at 0° or $2\theta_g$. Besides, for the wavelengths that verify $\Delta\varphi(\omega) = \pi/2 + \pi m$, the absolute value of ellipticity is maximum ($|\varepsilon| = \tan\theta_g$), reaching circular polarization ($\varepsilon = \pm 1$) only for the case of $\theta_g = 45°$ [Fig. 7(A3) and 8(A)] where the amplitudes are equal. The periodic variation of the polarization ellipse is faster in the case of two consecutive retarder plates (Fig. 8) than in the case of one retarder plate (Fig. 7, row 3), due to the higher delay between both polarization components.

The evolution of the polarization ellipse in the time domain is less intuitive than in the spectral domain. To visualize it better, we plot the temporal evolution of the vector electric field [Fig. 8(C) and 8(D)] of the pulse generated with two consecutive retarder plates. This pulse is almost linearly polarized ($\varepsilon \approx 0$) at its front and rear parts due to the high delay compared to the pulse duration, perpendicular between them ($\chi \approx 0°$ and $\chi \approx 90°$, respectively). In the intermediate part, the pulse describes a left-handed ellipse, being circular polarization ($\varepsilon = -1$) when the amplitudes of both components are the same. The retrieved and simulated results show a good agreement in the regions with non-negligible pulse intensity.

5. Conclusions

We have characterized complex ultrashort vector pulses, which exhibit time- (and frequency-) varying polarization, from a single amplitude swing trace measurement. For this purpose, we have demonstrated analytically, numerically, and experimentally that all the information needed to characterize vector pulses is codified in the amplitude swing trace. Subsequently, we have developed a reconstruction strategy to extract this information, validating it both numerically and experimentally. This way, the amplitude swing capability to measure vector pulses is proven.

Optics EXPRESS

Vector pulses are characterized by the spectral amplitudes (experimentally recorded) and phases of two polarization components, including their relative phase. We have analyzed the diverse terms contributing to the amplitude swing trace and identified those codifying both polarization projections spectral phases and their relative phase. The developed reconstruction strategy used to extract the pulse information from the measured trace is based on several steps of a nonlinear optimization algorithm (in our case, the Levenberg-Marquardt, but any other could be used). We have applied this strategy to retrieve vector pulses experimentally generated by propagating linearly polarized pulses through different retarder plates. By simulating this propagation, we validate the measured pulses. We find a good agreement between simulated and retrieved pulses, even when there is a small temporal overlap between both polarization components.

In sum, it is possible to completely reconstruct a complex vector pulse from a single amplitude swing trace. This trace can be measured with a simple and compact in-line setup, with common and inexpensive optical elements, and can benefit from other advantages of amplitude swing (e.g., flexibility in pulse bandwidth, chirp, or broad spectral region of application).

Funding. Ministerio de Ciencia e Innovación (PID2020-119818GB-I00); Ministerio de Economía y Competitividad (EQC2018-004117-P); Junta de Castilla y León (SA136-P20).

Acknowledgements. C. Barbero acknowledges the support from Junta de Castilla y León and Fondo Social Europeo Plus through their Ph. D. grant program.

Disclosures. B. Alonso and Í. J. Sola have patent # WO/2021/123481 pending to University of Salamanca**.**

Data availability. Data underlying the results presented in this paper are not publicly available at this time but may be obtained from the authors upon reasonable request**.**

Supplemental document. See Supplement 1 for supporting content.

References

1. K. Misawa, "Applications of polarization-shaped femtosecond laser pulses," Adv. Phys.: X **1**(4), 544–569 (2016).
2. H. Rhee, Y. G. June, J. S. Lee, *et al.*, "Femtosecond characterization of vibrational optical activity of chiral molecules," Nature **458**(7236), 310–313 (2009).
3. O. Varela, A. Zaïr, J. San Román, *et al.*, "Above-millijoule super-continuum generation using polarisation dependent filamentation in atoms and molecules," Opt. Express **17**(5), 3630–3639 (2009).
4. X. Chen, A. Jullien, A. Malvache, *et al.*, "Generation of 43 fs, 1 mJ laser pulses via compression of circularly polarized pulses in a gas-filled hollow-core fiber," Opt. Lett. **34**(10), 1588 (2009).
5. Q. Wu, L. Gao, Y. Cao, *et al.*, "Single-shot measurement of wavelength-resolved state of polarization dynamics in ultrafast lasers using dispersed division-of-amplitude," Photonics Res. **11**(1), 35 (2023).
6. Y. Long, Q. Wu, Z. Chang, *et al.*, "Experimental study of single-shot polarization dynamics of dual dissipative solitons," Opt. Laser Technol. **161**, 109190 (2023).
7. A. Forbes, M. de Oliveira, and M. R. Dennis, "Structured light," Nat. Photonics **15**(4), 253–262 (2021).
8. B. Alonso, I. López-Quintás, W. Holgado, *et al.*, "Complete spatiotemporal and polarization characterization of ultrafast vector beams," Commun. Phys. **3**(1), 151 (2020).
9. Í. J. Sola, E. Mével, L. Elouga, *et al.*, "Controlling attosecond electron dynamics by phase-stabilized polarization gating," Nat. Phys. **2**(5), 319–322 (2006).
10. D. J. Kane and R. Trebino, "Characterization of arbitrary femtosecond pulses using frequency-resolved optical gating," IEEE J. Quantum Electron. **29**(2), 571–579 (1993).
11. C. Iaconis and I. A. Walmsley, "Spectral phase interferometry for direct electric-field reconstruction of ultrashort optical pulses," Opt. Lett. **23**(10), 792–794 (1998).
12. M. Miranda, T. Fordell, C. Arnold, *et al.*, "Simultaneous compression and characterization of ultrashort laser pulses using chirped mirrors and glass wedges," Opt. Express **20**(1), 688–697 (2012).
13. B. Alonso, W. Holgado, and Í. J. Sola, "Compact in-line temporal measurement of laser pulses with amplitude swing," Opt. Express **28**(10), 15625–15640 (2020).
14. A. Leblanc, P. Lassonde, S. Petit, *et al.*, "Phase-matching-free pulse retrieval based on transient absorption in solids," Opt. Express **27**(20), 28998 (2019).
15. W. J. Walecki, D. N. Fittinghoff, A. L. Smirl, *et al.*, "Characterization of the polarization state of weak ultrashort coherent signals by dual-channel spectral interferometry," Opt. Lett. **22**(2), 81–83 (1997).
16. L. Lepetit, G. Chériaux, and M. Joffre, "Linear techniques of phase measurement by femtosecond spectral interferometry for applications in spectroscopy," J. Opt. Soc. Am. B **12**(12), 2467–2474 (1995).
17. B. Alonso and Í. J. Sola, "Measurement of ultrashort vector pulses from polarization gates by in-line, single-channel spectral interferometry," IEEE J. Quantum Electron. **25**(4), 8900307 (2019).

Optics EXPRESS

18. P. Schlup, O. Masihzadeh, L. Xu, *et al.*, "Tomographic retrieval of the polarization state of an ultrafast laser pulse," Opt. Lett. **33**(3), 267–269 (2008).
19. D. D. Rivas, A.-K. Raab, C. Guo, *et al.*, "Measurement of ultrashort laser pulses with a time-dependent polarization state using the d-scan technique," JPhys Photonics **6**(1), 015003 (2024).
20. M. T. Seidel, Z. Zhang, S. Yan, *et al.*, "Characterization of polarization shaped ultraviolet femtosecond laser pulses," J. Opt. Soc. Am. B **28**(11), 2718 (2011).
21. S. Linden, H. Giessen, and J. Kuhl, "XFROG - A new method for amplitude and phase characterization of weak ultrashort pulses," Phys. Status Solidi B **206**(1), 119–124 (1998).
22. G. E. Jellison and D. H. Lowndes, "Time-resolved ellipsometry," Appl. Opt. **24**(18), 2948–2955 (1985).
23. J. Bai, C. Wang, X. Chen, *et al.*, "Chip-integrated plasmonic flat optics for mid-infrared full-Stokes polarization detection," Photonics Res. **7**(9), 1051 (2019).
24. T. Bauer, S. Orlov, U. Peschel, *et al.*, "Nanointerferometric amplitude and phase reconstruction of tightly focused vector beams," Nat. Photonics **8**(1), 23–27 (2014).
25. Í. J. Sola and B. Alonso, "Robustness and capabilities of ultrashort laser pulses characterization with amplitude swing," Sci. Rep. **10**(1), 18364 (2020).
26. M. López-Ripa, Í. J. Sola, and B. Alonso, "Amplitude swing ultrashort pulse characterization across visible to near-infrared," Opt. Laser Technol. **164**, 109492 (2023).
27. M. López-Ripa, Í. J. Sola, and B. Alonso, "Generalizing amplitude swing modulation for versatile ultrashort pulse measurement," Opt. Express **31**(21), 34428–34442 (2023).
28. I. Will, P. Nickles, M. Schnuerer, *et al.*, "Compact FROG system useful for measurement of multiterawatt laser pulses," Opt. Commun. **132**(1-2), 101–106 (1996).
29. A. S. Radunsky, I. A. Walmsley, S.-P. Gorza, *et al.*, "Compact spectral shearing interferometer for ultrashort pulse characterization," Opt. Lett. **32**(2), 181–183 (2007).
30. T. Oksenhendler, S. Coudreau, N. Forget, *et al.*, "Self-referenced spectral interferometry," Appl. Phys. B **99**(1-2), 7–12 (2010).
31. G. Ghosh, "Dispersion-equation coefficients for the refractive index and birefringence of calcite and quartz crystals," Opt. Commun. **163**(1-3), 95–102 (1999).
32. M. Miranda, J. Penedones, C. Guo, *et al.*, "Fast iterative retrieval algorithm for ultrashort pulse characterization using dispersion scans," J. Opt. Soc. Am. B **34**(1), 190–197 (2017).
33. E. Escoto, A. Tajalli, T. Nagy, *et al.*, "Advanced phase retrieval for dispersion scan: a comparative study," J. Opt. Soc. Am. B **35**(1), 8–19 (2018).
34. T. Zahavy, A. Dikopoltsev, D. Moss, *et al.*, "Deep learning reconstruction of ultrashort pulses," Optica **5**(5), 666–673 (2018).
35. S. Kleinert, A. Tajalli, T. Nagy, *et al.*, "Rapid phase retrieval of ultrashort pulses from dispersion scan traces using deep neural networks," Opt. Lett. **44**(4), 979–982 (2019).
36. K. Levenberg, "A method for the solution of certain non-linear problems in least squares," Q. Appl. Math. **2**(2), 164–168 (1944).
37. D. W. Marquardt, "An algorithm for least-squares estimation of nonlinear parameters," J. Soc. Ind. Appl. Math. **11**(2), 431–441 (1963).
38. B. Alonso, Í. J. Sola, and H. Crespo, "Self-calibrating d-scan: Measuring ultrashort laser pulses on-Target using an arbitrary pulse compressor," Sci. Rep. **8**(1), 3264 (2018).
39. F. Silva, B. Alonso, W. Holgado, *et al.*, "Strategies for achieving intense single-cycle pulses with in-line post-compression setups," Opt. Lett. **43**(2), 337–340 (2018).
40. B. Alonso, S. Torres-Peiró, R. Romero, *et al.*, "Detection and elimination of pulse train instabilities in broadband fibre lasers using dispersion scan," Sci. Rep. **10**(1), 7242 (2020).